

Light-triggered regionally controlled n-doping of organic semiconductors

<https://doi.org/10.1038/s41586-025-09075-y>

Received: 20 January 2023

Accepted: 28 April 2025

Published online: 28 May 2025

 Check for updates

Xin-Yi Wang¹, Yi-Fan Ding¹, Xiao-Yan Zhang¹, Yang-Yang Zhou¹, Chen-Kai Pan¹, Yuan-He Li¹, Nai-Fu Liu¹, Ze-Fan Yao¹, Yong-Shi Chen¹, Zhi-Hao Xie¹, Yi-Fan Huang¹, Yu-Chun Xu¹, Hao-Tian Wu¹, Chun-Xi Huang¹, Miao Xiong¹, Li Ding¹, Zi-Di Yu¹, Qi-Yi Li¹, Yu-Qing Zheng², Jie-Yu Wang¹ & Jian Pei¹✉

Doping is a primary method to modulate the electrical properties of semiconductors, enabling the fabrication of various homojunctions/heterojunctions and complex devices^{1–8}. For organic semiconductors (OSCs), the electrical performance has been extensively improved by developing doping methods and dopants^{9–13}. However, compared with the state-of-the-art spatial resolution of inorganic semiconductor fabrication processes, OSCs lag far behind, limiting the construction of complex organic electronic devices⁵. Here we present a facile light-triggered doping strategy and develop a series of inactive photoactivable dopants (iPADs) for regionally controlled n-doping of OSCs. By converting iPADs into active dopants through ultraviolet (UV) exposure, controllable doping of various n-type OSCs with high electrical conductivity greater than 30 S cm^{-1} has been realized. Using iPADs can substantially improve the performances of OSCs in transistors, logic circuits and thermoelectrics. Also, regionally controlled doping is demonstrated in OSCs with a record resolution down to $1 \mu\text{m}$. Overall, our strategy has achieved tunable doping levels in OSCs with high spatial resolution, which is expected to be highly suited for integrated circuits in both roll-to-roll and laboratory-scale environments.

Regionally controlled doping of silicon with high resolution forms the basis for the modern electronics industry. Similarly, developing doping methods with high spatial resolution in OSCs can accelerate the fabrication of organic integrated circuits containing interconnects, electrodes, p–n junctions^{14–16} and so on. Precisely, regionally controlled doping channels and contacts of organic field-effect transistors (FETs) can fill traps, modulate charge transport polarity and achieve ohmic contacts, which are indispensable in improving device performance and downscaling devices^{17–23}. However, in traditional methods, doping reactions typically occur spontaneously once mixing or depositing dopants with OSCs, severely limiting the spatial resolution²³. Fabrication techniques such as inkjet printing and thermal evaporation can deposit dopants onto the specific regions of OSC films by external space confinement, but the resolution barely meets the requirement of integrated circuits²⁴. Consequently, there is an urgent need to develop inert dopants that can be activated through external stimuli to regionally dope OSCs with a potential micrometre-level or submicrometre-level resolution.

Photochemical reactions play an important role in the semiconductor industry, for example, photolithography, for achieving high-resolution patterns^{25–27}. Therefore, the light-triggered doping method is expected to potentially pattern conductive regions with high resolution, high uniformity and high yield. Some studies have achieved weak n-doping/p-doping of OSCs by photoinduced electron/

hole transfer^{28–36} (Fig. 1a). However, dopants that can dope OSCs with high doping ability and resolution through only light triggering have yet to be reported (Supplementary Tables 1 and 2).

Here a new class of light-triggered n-dopants with unique thermal stability, UV light sensitivity and strong and irreversible n-doping ability is designed to realize regionally controlled n-doping of OSCs. The untriggered dopants, named iPADs (Fig. 1a,b), transform into highly reactive photoactivated dopants (PADs) with light irradiation. Regional light illumination lets iPADs dope various n-type OSCs in a regionally controlled manner (Fig. 1c,d). The high spatial resolution down to $1 \mu\text{m}$ has been demonstrated and further applied in organic electronic devices, showing potential application in integrated circuits and printable electronics.

Light-triggered n-doping

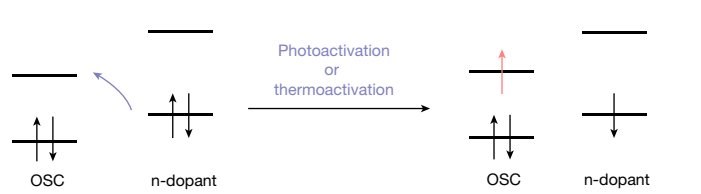
iPADs undergo light-triggered 6π -electrocyclization processes to form active dopants, PADs, which readily aromatize to PAD⁺s by n-doping OSCs through irreversible hydride-transfer processes^{37,38} (Extended Data Figs. 1 and 2). Density functional theory (DFT) calculation indicates that iPADs can transform into PADs instantly after light exposure at room temperature, whereas the transformation is infeasible through thermoactivation (Supplementary Figs. 1 and 2). Meanwhile, PADs exhibit the lowest activation energy of doping reaction compared

¹Beijing National Laboratory for Molecular Sciences (BNLMS), Key Laboratory of Polymer Chemistry and Physics of Ministry of Education, Center of Soft Matter Science and Engineering, College of Chemistry and Molecular Engineering, Peking University, Beijing, People's Republic of China. ²National Key Laboratory of Advanced Micro and Nano Manufacture Technology, School of Integrated Circuits, Peking University, Beijing, People's Republic of China. ✉e-mail: jianpei@pku.edu.cn

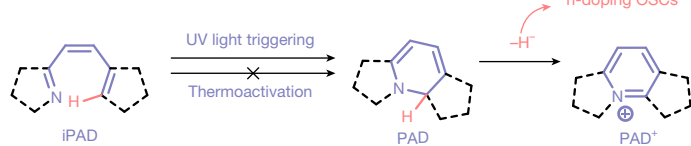
Article

a Light-triggered n-doping mechanism

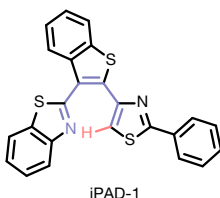
Previous work



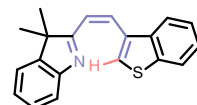
This work



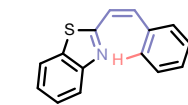
b iPADs



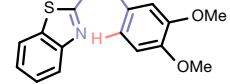
iPAD-1



Z-iPAD-2

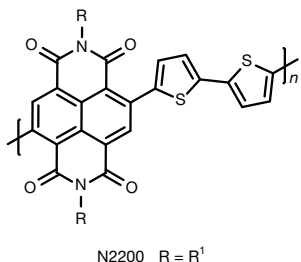


Z-iPAD-3

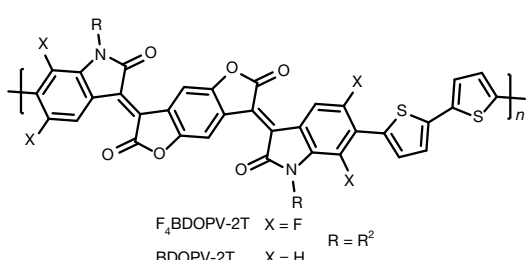


Z-iPAD-4

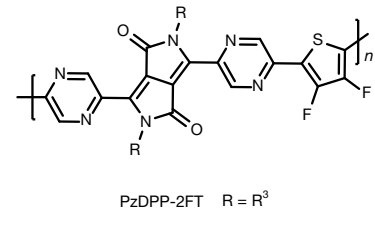
c n-Type OSCs



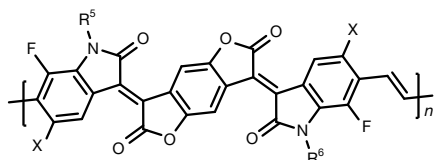
N2200 R = R¹



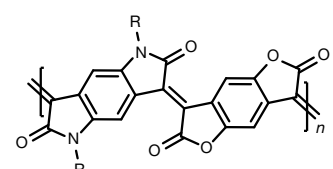
F₄BDOPV-2T X = F
BDOPV-2T X = H R = R²



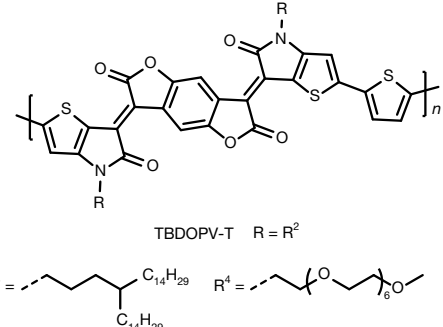
P2DPP-2FT R = R³



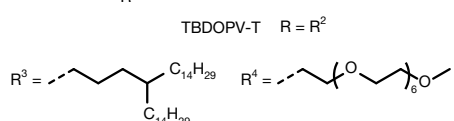
FBDPPV X = H R⁵ = R⁶ = R²
FBDPPV-OEG X = H R⁵ = R⁶ = R⁴
UFBDPPV X = H R⁵ = R²; R⁶ = R⁴
F₄BDPPV X = F R⁵ = R⁶ = R²



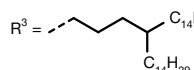
LPPV R = R¹



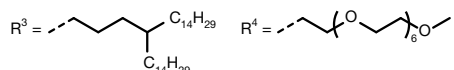
TBDOPV-T R = R²



R¹ = 2-octyldodecyl R² = C₁₈H₃₇ C₁₈H₃₇



R³ = C₁₄H₂₉ C₁₄H₂₉



R⁴ = C₁₄H₂₉ C₁₄H₂₉

d Light-triggered n-doping method

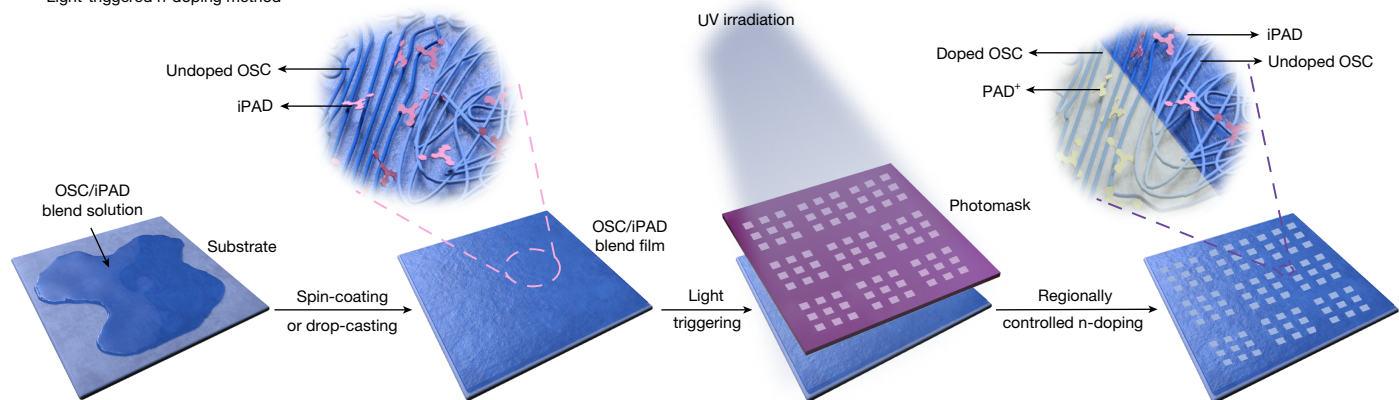


Fig. 1 | Light-triggered doping method. **a**, Traditional photoactivated and thermoactivated doping processes and light-triggered doping methods in this work. **b,c**, Chemical structures of designed iPADs (**b**) and adopted OSCs (**c**) in this study. **d**, Schematics of the light-triggered doping method. OSCs are

directly mixed with iPADs to fabricate films by spin-coating or drop-casting, followed by a light-triggered transformation of iPADs to highly active PADs for regionally controlled n-doping of OSCs.

with other reported n-dopants, indicating high doping reactivity (Supplementary Fig. 3).

The light-triggered doping process is demonstrated by iPAD-1 with FBDPPV, a representative n-type OSC. After UV irradiation (365 nm)

on blend solution, polaronic absorptions (from 900 to 2,000 nm) of FBDPPV gradually appeared (Fig. 2a). The doping ability of iPAD-1 is on par with the commonly used high-activity n-dopants such as (4-(1,3-dimethyl-2,3-dihydro-1*H*-benzimidazol-2-yl)phenyl)dimethylamine

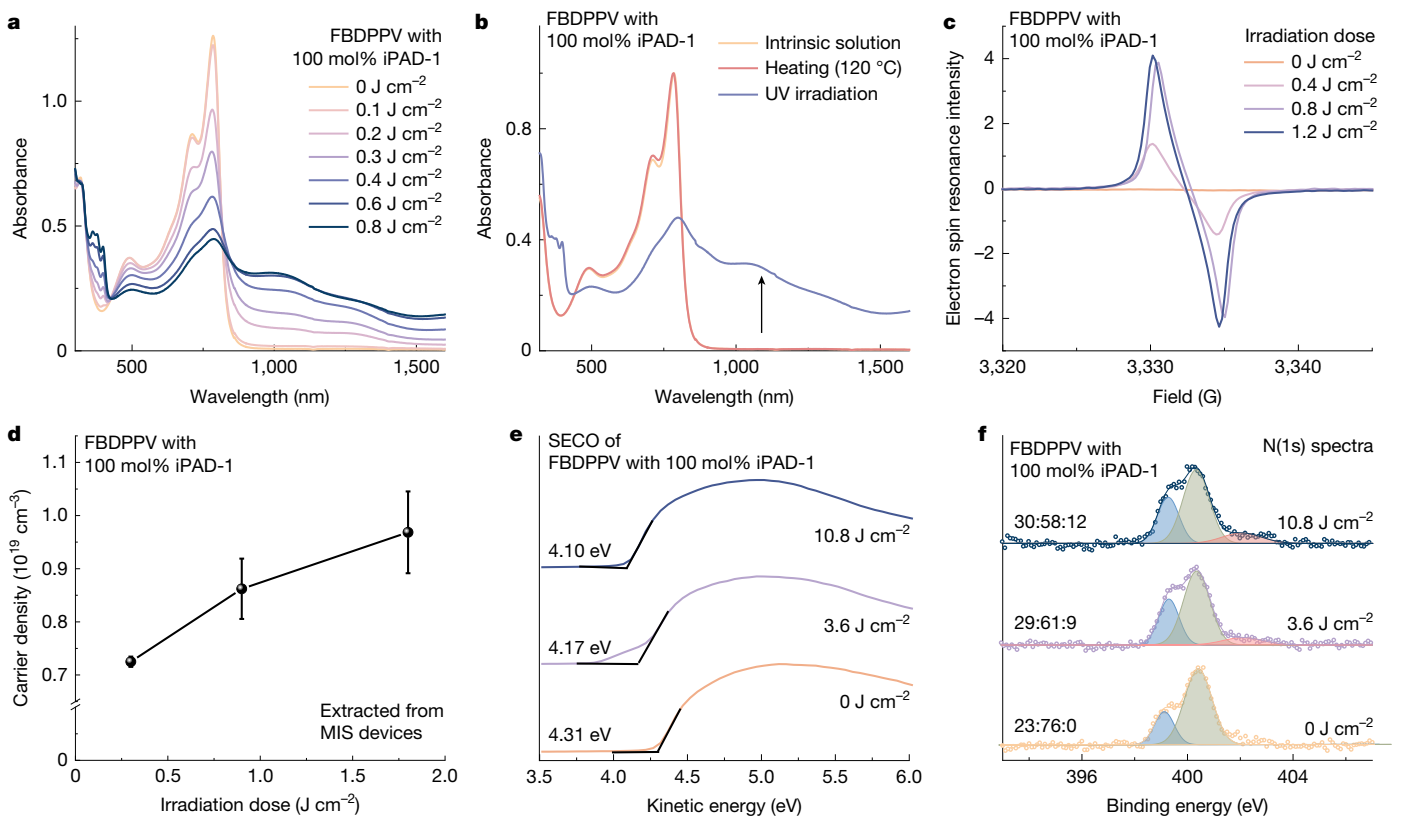


Fig. 2 | Light-triggered n-doping. **a**, In situ UV-vis-NIR absorption spectra of FBDPPV/100 mol% iPAD-1 mixtures in chlorobenzene under UV irradiation. **b**, In situ UV-vis-NIR spectra of FBDPPV/100 mol% iPAD-1 mixtures in chlorobenzene after heating at 120 °C for 10 min or after 0.8 J cm⁻² UV irradiation. **c**, EPR spectra of FBDPPV/100 mol% iPAD-1 films before and after UV irradiation. **d**, Carrier density extracted from metal-insulator-semiconductor (MIS) devices. Carrier concentration of blend film is extremely low before UV irradiation, unable to be tested by MIS devices. Points, mean; error bars, s.d.; $n = 3$ independent samples. **e**, Secondary electron cut-off (SECO) of FBDPPV/100 mol% iPAD-1 films before and after UV irradiation. **f**, N(1s) XPS spectra of 100 mol% PAD-1-doped FBDPPV films before and after UV irradiation.

(N-DMBI), indicating the high doping activity of PAD-1 (Supplementary Figs. 4 and 5). Meanwhile, absorption spectra also show that iPAD-1 cannot dope FBDPPV without light irradiation even when heated at 120 °C (Fig. 2b). The orthogonality between thermal and photochemical processes provides a wide temperature window for reliable device fabrication. The increase of spin density from electron paramagnetic resonance (EPR) spectroscopy of FBDPPV/iPAD-1 blend suggests the generation of polaron after UV irradiation, which is consistent with absorption spectra (Fig. 2c and Supplementary Fig. 7). Mott-Schottky analysis further confirms the positive correlation between the free-carrier density of doped FBDPPV and irradiation dose (Fig. 2d and Supplementary Fig. 8). The carrier density measured by Mott-Schottky analysis is about 10^{19} cm⁻³, comparable with the spin density measured by EPR, suggesting the high doping ability of iPAD-1. The work function of FBDPPV/iPAD-1 blend film evaluated by UV photoelectron spectroscopy (UPS) shows an apparent decrease of 0.14 and 0.21 eV under exposure doses of 3.6 and 10.8 J cm⁻², respectively, indicating modulation of the Fermi level of OSCs by light-triggered doping (Fig. 2e and Supplementary Fig. 9). N(1s) spectra of X-ray photoelectron spectroscopy (XPS) measurements show quadrivalent nitrogen signals at 402 eV in FBDPPV/iPAD-1 film after UV irradiation, indicating the generation of PAD-1⁺ (Fig. 2f). Meanwhile, the effective doping at film depth of more than 1 μm has also been demonstrated by XPS (Supplementary Fig. 10). Grazing incidence wide-angle X-ray scattering suggests that iPAD-1 barely affects the molecular packing of FBDPPV, implying the excellent miscibility between iPADs and OSCs, which has also been proved by atomic force microscopy (AFM) images and FETs (Supplementary Figs. 11–13). Therefore, the above results have confirmed that iPADs can serve as a catalogue of dopants for light-triggered n-doping of OSCs.

Generality of light-triggered n-doping

The generality of light-triggered doping capabilities is explored by using four iPADs. The doping kinetics of four iPADs, which were measured with a representative hydride acceptor, (MeO)₃Tr⁺, and a representative polymer, FBDPPV, follow the tendency iPAD-2 > iPAD-1 > iPAD-3 and iPAD-4, according to UV-visible-near infrared (UV-vis-NIR) spectra and DFT calculation (Fig. 3a,b, Extended Data Fig. 3 and Supplementary Figs. 14–18). We discovered that the electrical conductivity of the doped film depends on the reactivity of dopants. The maximum conductivity of FBDPPV/iPAD-2 blend film reaches 1.1 S cm⁻¹, which is higher than 0.2 S cm⁻¹ for FBDPPV/iPAD-1 blends and 10⁻⁴ S cm⁻¹ for FBDPPV/iPAD-3 and FBDPPV/iPAD-4 blends (Fig. 3c), owing to the higher doping reactivity and smaller molecular size of iPAD-2 (Supplementary Fig. 16).

After that, we investigated the generality of the light-triggered n-doping process by using ten types of OSC with different lowest unoccupied molecular orbital (LUMO) levels (-3.7 to -4.7 eV) (Extended Data Fig. 2 and Supplementary Fig. 19). Before UV irradiation, OSC/iPAD blend films show similar low conductivity as pristine OSCs (Supplementary Table 4). After exposure to UV irradiation, the conductivities of various OSC/iPAD blend systems improve by 3 to 9 orders of magnitude without further annealing procedures (Fig. 3d,e, Supplementary Figs. 20–22 and Supplementary Table 5). Conductivity, doping level and Fermi level of blend films can be precisely dual-modulated by irradiation doses and dopant molar ratios (Supplementary Fig. 23). Among all OSC/iPAD blends, TBDOPV-T/iPAD-2 shows the highest conductivity of 31 S cm⁻¹ under a UV exposure dose of 1.1 J cm⁻². For the widely investigated n-type OSC (N2200), the conductivity, doping level and thermal stability of iPAD-doped films are comparable and even higher than those

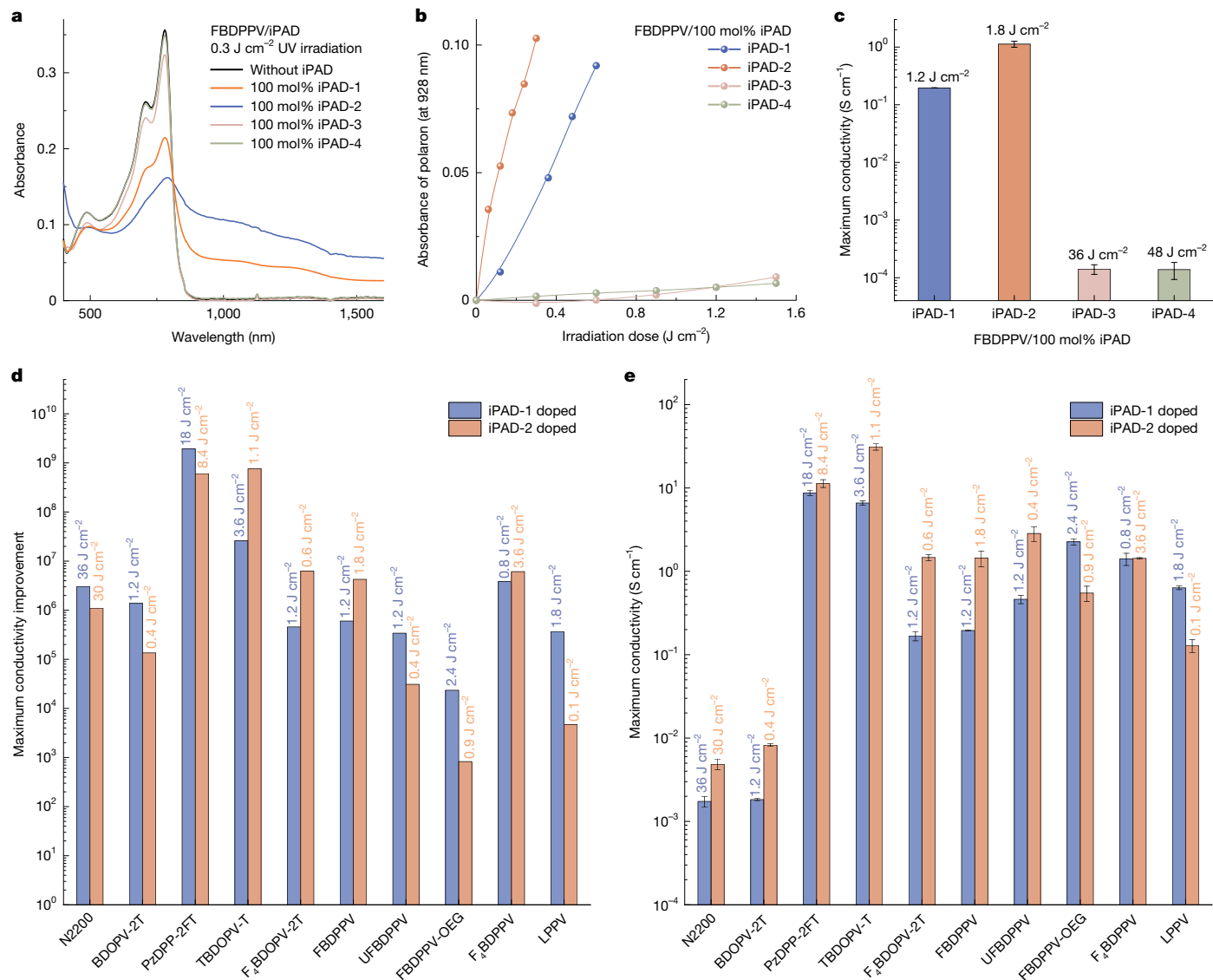


Fig. 3 | Generality of light-triggered n-doping. **a**, UV-vis-NIR spectra of FBDPPV with or without 100 mol% of four iPADs, respectively. **b**, Irradiation-dose-dependent absorbance of polaron at 928 nm for the four FBDPPV/iPAD blends. **c**, Maximum conductivities of iPAD-doped FBDPPV with different irradiation doses. Boxes, mean; error bars, s.d.; $n = 3$ independent samples. **d**, Maximum conductivity improvements and corresponding UV irradiation

dose of OSCs by light-triggered doping, which are calculated by dividing the maximum conductivities of blend films after UV irradiation by those before UV irradiation. **e**, Maximum conductivities and corresponding UV irradiation dose of OSCs by light-triggered doping. Boxes, mean; error bars, s.d.; $n = 3$ independent samples.

doped by *N*-DMBI or ruthenium organometallic dimer ($[\text{RuCp}^*\text{Mes}]_2$) (Supplementary Figs. 24 and 25). The above experiments indicate the powerful doping abilities of iPADs and the generalities of light-triggered doping processes.

Applications of light-triggered n-doping

The inactive light-triggered dopants (iPADs) experimentally show high solubilities in commonly used organic solvents ($>1 \text{ g l}^{-1}$), excellent thermal stability (up to 200 °C) and outstanding air stability (more than half a year in solid state and at least 5 days in CDCl_3 solution), facilitating the construction of large-scale integrated circuits with exceptional performance³⁹ (Supplementary Figs. 26–28). Here channel-doped FETs using FBDPPV/iPAD-2 blends as the active layer have been fabricated. Selectively doping the channel of FETs has been reported to effectively fill the carrier traps in the channel and lower the energy barrier of carrier transport⁴⁰. Electron mobilities of FETs gradually increase,

whereas surface traps decrease with the irradiation dose (Fig. 4a–c, Extended Data Fig. 4, Supplementary Figs. 29–36 and Supplementary Table 6). Furthermore, by optimizing exposure doses (0–0.14 J cm⁻²) and dopant molar ratios (0.01–0.03 mol%), electron mobilities of FETs increase to $0.71 \pm 0.36 \text{ cm}^2 \text{ V}^{-1} \text{ s}^{-1}$ for FBDPPV/0.02 mol% iPAD-2 blend after 0.1 J cm⁻² UV irradiation and $4 \times 10^{11} \text{ cm}^{-2}$ surface traps are eliminated for FBDPPV/0.03 mol% iPAD-2 blend after 0.1 J cm⁻² UV irradiation (Extended Data Fig. 4). Doping the contacts of FETs can reduce contact resistance and eliminate the energy barrier for carrier injection⁴⁰. After light-triggered doping on contacts, nonideal behaviours of FETs with short channels ($L = 5 \mu\text{m}$) have attenuated, whereas the mobilities increase and the threshold voltages decrease (Fig. 4d, Extended Data Fig. 5, Supplementary Figs. 38–43 and Supplementary Table 7). Specifically, the on–off ratios of FETs are at 10^5 after doping, indicating that the light-triggered doping reaction only occurs at contacts. The contact resistance of FETs at $V_G = 80 \text{ V}$ is reduced from 10 kΩ cm to 1.5 kΩ cm, whereas transfer length (L_T) is shortened from

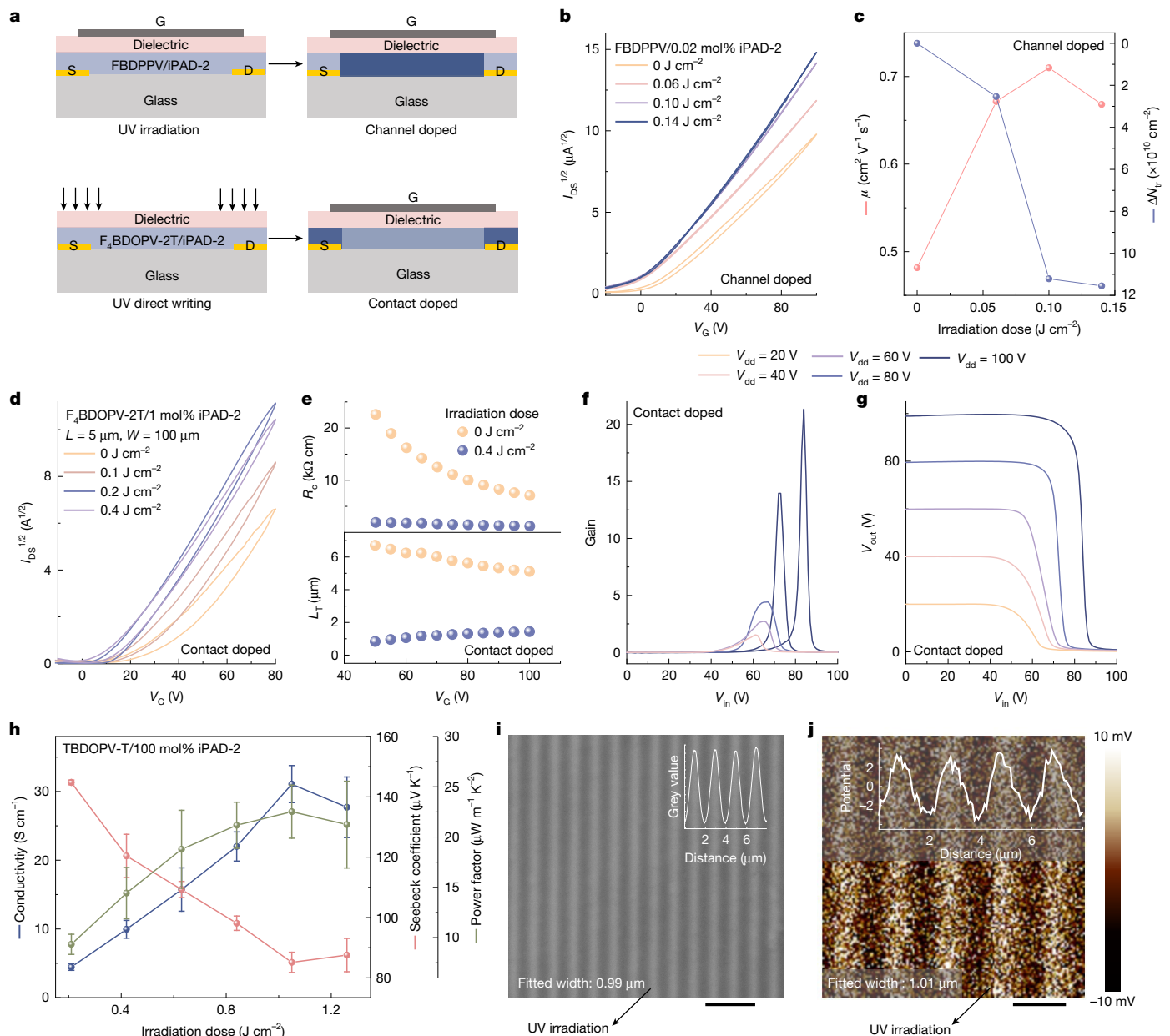


Fig. 4 | Applications of the light-triggered doping method. **a**, Light-triggered doping of FETs at channels and contacts. Channel-doped FETs are fabricated using FBDPPV/iPAD-2 blends as active layers. FBDPPV is selected as the channel material owing to the disordered packing structure and high trap density. **b,c**, Transfer characteristics, mobilities and relative surface trap densities of FETs at different UV exposure doses ($V_{DS} = 100\text{ V}$, saturated regime). Points, mean; $n = 5$ independent samples. Mobilities, threshold voltages and I_{on}/I_{off} of FETs using pristine and light-triggered doped FBDPPV are summarized in Supplementary Table 7. Contact-doped FETs are fabricated using $F_4BDOPV\text{-}2T/iPAD\text{-}2$ blends as active layers. $F_4BDOPV\text{-}2T$ is selected as the channel material owing to the severe nonideal behaviours. **d**, Transfer characteristics for FETs with $L = 5\text{ }\mu\text{m}$ ($V_{DS} = 80\text{ V}$, saturated regime). Mobilities, threshold voltages and I_{on}/I_{off} of FETs using pristine and light-triggered doped $F_4BDOPV\text{-}2T$ are summarized in Supplementary Table 7. Points, mean; $n = 5$ independent samples.

e, Transfer lengths and contact resistances of devices measured by the transfer-line method before and after UV irradiation. **f,g**, Gain values (**f**) and static switching characteristics (**g**) of an inverter at different voltages. $F_4BDOPV\text{-}2T/1\text{ mol\% iPAD-2}$ blend serves as the n-channel material. DPP-TVT serves as the p-channel material. **h**, Conductivities, Seebeck coefficients and power factors of TBDOPV-T/iPAD-2 blend films. Points, mean; error bars, s.d.; $n = 3$ independent samples. TBDOPV-T is chosen to fabricate thermoelectric devices owing to the high thermoelectric performance. **i**, Optical image of PzDPP-2T/iPAD-1 blend film patterned with an array of $1\text{ }\mu\text{m}$. Because doping can bleach the colour of OSCs, an n-type polymer of PzDPP-2FT used here changes from dark to grey after doping. The inset line represents the grey value of the patterned array. Scale bar, $5\text{ }\mu\text{m}$. **j**, KPFM images of patterned doped lines with a width of $1\text{ }\mu\text{m}$. Scale bar, $2\text{ }\mu\text{m}$.

$5.6\text{ }\mu\text{m}$ to $1.3\text{ }\mu\text{m}$ after light-triggered doping, beneficial for downscaling FET devices (Fig. 4e and Supplementary Fig. 44). Furthermore, a complementary inverter using FETs with iPADs shows enhanced gain values from 10 to 22 after light-triggered contact doping (Fig. 4f,g and Extended Data Fig. 5j–m), showing the potential application of iPADs in organic logic circuits.

iPADs are also applied in electronic devices that require high carrier concentration, such as thermoelectric devices and electronic circuits. A power factor of $22.5\text{ }\mu\text{W m}^{-1}\text{K}^{-2}$ is achieved in the TBDOPV-T/iPAD-2 blend at 1.1 J cm^{-2} UV radiation dose, facilitating the regionally controlled construction of the n-leg in thermoelectric devices by UV irradiation (Fig. 4h and Supplementary Fig. 45). Owing to the high

doping ability and light-triggered properties of the OSC/iPAD blend systems, wires, electrodes and other conductive patterns are conveniently fabricated by UV irradiation. A simple circuit using TBDOPV-T/iPAD-2 blend to control the LED bulbs has been constructed as a demonstration (Extended Data Fig. 6 and Supplementary Video 1). Also, the light-triggered doping process can be performed on flexible polyimide substrates (Extended Data Fig. 6), showing the feasibility of applying iPADs in flexible optoelectronic devices.

Clear patterns of 1- μm arrays of doped areas on OSC/iPAD blend films are observed by optical microscopy and Kelvin probe force microscopy (KPFM) after regionally controlled UV exposure (Fig. 4*i,j* and Supplementary Figs. 46 and 47). The high spatial resolution of our light-triggered doping method is also supported by the conductive atomic force microscopy (C-AFM) image (Supplementary Fig. 48). Furthermore, the patterns with 1 μm spatial resolution exhibited high stability in 7 days owing to the high doping activity of PADs (Supplementary Figs. 47 and 49). Overall, we confirm that our light-triggered doping method has a high resolution better than 1 μm . We predict that the light-triggered doping method may allow higher spatial resolution down to the submicrometre level with the help of advanced high-resolution exposure methods.

Concluding remarks

In conclusion, we have successfully developed a unique strategy for regionally controlled doping of OSCs with superfine feature size. The strategy comprises two key components: a facile light-triggered doping method that enables high-resolution regionally controlled doping and a series of light-triggered n-dopants that fully harness the potential of the doping method. These components are interdependent and complement each other, contributing to the success of the strategy. Four light-triggered n-dopants have been developed to universally dope ten different OSCs with conductivity improved by 9 orders of magnitude using light alone. Compatible with modern high-resolution photolithography techniques, our strategy achieves a record high resolution of 1 μm in n-doping of OSCs. Notably, the resolution is expected to achieve a submicrometre scale with improved light exposure technique. Several fundamental organic electronic devices, such as FETs, logic circuits and thermoelectric devices, have been fabricated and light-triggered doped to achieve state-of-the-art performance. Specifically, through high-resolution contact doping, the contact resistance of FETs is decreased by six times, whereas transfer length is shortened by four times, showing the potential application in downscaling FET devices. Furthermore, our doping method is decoupled from other critical device fabrication processes, such as solution preparation, film deposition and thermal annealing, making it suitable for the fabrication procedures of integrated circuits. As a general strategy for doping OSCs, our dopants provide a feasible approach for the application of OSCs in the multistep fabrication processes of very-large-scale integration.

Online content

Any methods, additional references, Nature Portfolio reporting summaries, source data, extended data, supplementary information, acknowledgements, peer review information; details of author contributions and competing interests; and statements of data and code availability are available at <https://doi.org/10.1038/s41586-025-09075-y>.

- Talin, A. A. et al. Tunable electrical conductivity in metal-organic framework thin-film devices. *Science* **343**, 66–69 (2014).
- Scaccabarozzi, A. D. et al. Doping approaches for organic semiconductors. *Chem. Rev.* **122**, 4420–4492 (2022).
- Russ, B., Glaudell, A., Urban, J. J., Chabinyc, M. L. & Segalman, R. A. Organic thermoelectric materials for energy harvesting and temperature control. *Nat. Rev. Mater.* **1**, 16050 (2016).

- Pfeiffer, M. et al. Doped organic semiconductors: physics and application in light emitting diodes. *Org. Electron.* **4**, 89–103 (2003).
- Lüssem, B. et al. Doped organic transistors. *Chem. Rev.* **116**, 13714–13751 (2016).
- Zhang, M., Tang, Z., Liu, X. & Van der Spiegel, J. Electronic neural interfaces. *Nat. Electron.* **3**, 191–200 (2020).
- Wang, M., Dong, R. & Feng, X. Two-dimensional conjugated metal–organic frameworks (2D c-MOFs): chemistry and function for MOFtronics. *Chem. Soc. Rev.* **50**, 2764–2793 (2021).
- Kolesov, V. A. et al. Solution-based electrical doping of semiconducting polymer films over a limited depth. *Nat. Mater.* **16**, 474–481 (2017).
- Yang, C.-Y. et al. A thermally activated and highly miscible dopant for n-type organic thermoelectrics. *Nat. Commun.* **11**, 3292 (2020).
- Yamashita, Y. et al. Efficient molecular doping of polymeric semiconductors driven by anion exchange. *Nature* **572**, 634–638 (2019).
- Kiefer, D. et al. Double doping of conjugated polymers with monomer molecular dopants. *Nat. Mater.* **18**, 149–155 (2019).
- Guo, H. et al. Transition metal-catalysed molecular n-doping of organic semiconductors. *Nature* **599**, 67–73 (2021).
- Fahlman, M. et al. Interfaces in organic electronics. *Nat. Rev. Mater.* **4**, 627–650 (2019).
- Menard, E. et al. Micro- and nanopatterning techniques for organic electronic and optoelectronic systems. *Chem. Rev.* **107**, 1117–1160 (2007).
- Chen, Y. et al. Selective doping of a single ambipolar organic semiconductor to obtain p- and n-type semiconductors. *Mater.* **5**, 2882–2897 (2022).
- Yu, Z.-D. et al. High n-type and p-type conductivities and power factors achieved in a single conjugated polymer. *Sci. Adv.* **9**, eadf3495 (2023).
- Guo, E. et al. Integrated complementary inverters and ring oscillators based on vertical-channel dual-base organic thin-film transistors. *Nat. Electron.* **4**, 588–594 (2021).
- Tang, C. G. et al. Doped polymer semiconductors with ultrahigh and ultralow work functions for ohmic contacts. *Nature* **539**, 536–540 (2016).
- Zeng, J. et al. Ultralow contact resistance in organic transistors via orbital hybridization. *Nat. Commun.* **14**, 324 (2023).
- Sawada, T. et al. Correlation between the static and dynamic responses of organic single-crystal field-effect transistors. *Nat. Commun.* **11**, 4839 (2020).
- Ante, F. et al. Contact resistance and megahertz operation of aggressively scaled organic transistors. *Small* **8**, 73–79 (2012).
- Klauk, H. Will we see gigahertz organic transistors? *Adv. Electron. Mater.* **4**, 1700474 (2018).
- Lüssem, B. et al. Doped organic transistors operating in the inversion and depletion regime. *Nat. Commun.* **4**, 2775 (2013).
- Zhao, W., Ding, J., Zou, Y., Di, C. & Zhu, D. Chemical doping of organic semiconductors for thermoelectric applications. *Chem. Soc. Rev.* **49**, 7210–7228 (2020).
- Zheng, Y.-Q. et al. Monolithic optical microlithography of high-density elastic circuits. *Science* **373**, 88–94 (2021).
- Jin, W. et al. Photocatalytic doping of organic semiconductors. *Nature* **630**, 96–101 (2024).
- Fukuzumi, S., Koumitsu, S., Hironaka, K. & Tanaka, T. Energetic comparison between photoinduced electron-transfer reactions from NADH model compounds to organic and inorganic oxidants and hydride-transfer reactions from NADH model compounds to p-benzoquinone derivatives. *J. Am. Chem. Soc.* **109**, 305–316 (1987).
- Schmidt, S. B. et al. Radical anion yield, stability, and electrical conductivity of naphthalene diimide copolymers n-doped with tertiary amines. *ACS Appl. Polym. Mater.* **2**, 1954–1963 (2020).
- Zhuo, J. et al. Direct spectroscopic evidence for a photodoping mechanism in polythiophene and poly(bithiophene-alt-thienothiophene) organic semiconductor thin films involving oxygen and sorbed moisture. *Adv. Mater.* **21**, 4747–4752 (2009).
- Lin, X. et al. Beating the thermodynamic limit with photo-activation of n-doping in organic semiconductors. *Nat. Mater.* **16**, 1209–1215 (2017).
- Mohapatra, S. K., Marder, S. R. & Barlow, S. Organometallic and organic dimers: moderately air-stable, yet highly reducing, n-dopants. *Acc. Chem. Res.* **55**, 319–332 (2022).
- Dobryden, I. et al. Dynamic self-stabilization in the electronic and nanomechanical properties of an organic polymer semiconductor. *Nat. Commun.* **13**, 3076 (2022).
- Kroon, R., Höfmann, A. I., Yu, L., Lund, A. & Müller, C. Thermally activated in situ doping enables solid-state processing of conducting polymers. *Chem. Mater.* **31**, 2770–2777 (2019).
- Chen, K. et al. Organic optoelectronic synapse based on photon-modulated electrochemical doping. *Nat. Photon.* **17**, 629–637 (2023).
- Hou, L. et al. Optically switchable organic light-emitting transistors. *Nat. Nanotechnol.* **14**, 347–353 (2019).
- Leydecker, T. et al. Flexible non-volatile optical memory thin-film transistor device with over 256 distinct levels based on an organic bicomponent blend. *Nat. Nanotechnol.* **11**, 769–775 (2016).
- Fedorova, O. A. et al. Photochemical electrocyclization of the indolinylphenylethenes involving a C–N bond formation. *Org. Lett.* **5**, 4533–4535 (2003).
- Martin, C. J. et al. Terarylenes as photoactivatable hydride donors. *J. Org. Chem.* **83**, 13700–13706 (2018).
- Wang, M. et al. Exceptionally high charge mobility in phthalocyanine-based poly(benzimidazobenzophenanthroline)-ladder-type two-dimensional conjugated polymers. *Nat. Mater.* **22**, 880–887 (2023).
- Xu, Y. et al. Doping: a key enabler for organic transistors. *Adv. Mater.* **30**, 13–19 (2018).

Publisher's note Springer Nature remains neutral with regard to jurisdictional claims in published maps and institutional affiliations.

Springer Nature or its licensor (e.g. a society or other partner) holds exclusive rights to this article under a publishing agreement with the author(s) or other rightsholder(s); author self-archiving of the accepted manuscript version of this article is solely governed by the terms of such publishing agreement and applicable law.

© The Author(s), under exclusive licence to Springer Nature Limited 2025

Methods

Material

OSCs used in this work were synthesized following procedures in the literature^{41–44}. Flexible polyimide substrates (CPI-TDS-C008) were provided by Ningbo Boya Poly Advanced Materials Co. Ltd.

Organic FETs

FETs with top gate/bottom contact architectures were fabricated using glass as substrates. Gold source and drain electrodes (with Cr as the adhesion layer) were patterned by photolithography. OSC/iPAD blend films were deposited on the treated substrates by spin-coating, optionally followed by thermal annealing. CYTOP (CTL-809M:CT-solv180 = 3:1) was coated by spin-casting onto OSC films to serve as the dielectric layer. Gate electrodes comprising a layer of Al (45 nm) were evaporated onto the dielectric layer through a shadow mask.

Conductivity and Seebeck coefficient measurements

Gold electrodes were pre-patterned by photolithography on the surface with a channel length of 200 μm and a channel width of 1,000 μm for conductivity measurements. OSC/iPAD blend films were deposited on the treated substrates by spin-coating, optionally followed by thermal annealing. Conductivity was measured by the four-probe method using the Keithley 4200-SCS semiconductor parameter analyser. The Seebeck coefficient was calculated by $S = \Delta V_{\text{therm}} / \Delta T$, in which ΔV_{therm} was the thermal voltage between the hot and cold ends of the device under a temperature difference (ΔT). ΔV_{therm} was monitored by the Keithley 4200-SCS. Temperature difference was introduced by a Joule heater and a cooling system.

UPS and XPS

UPS and XPS measurements were carried out by Kratos Axis Ultra DLD photoelectron spectrometer under an ultrahigh vacuum of about 3×10^{-9} Torr with an unfiltered He gas discharge lamp source (21.2 eV) and monochromatic Al Kα source (1,486.6 eV) as the excitation source. The instrumental energy resolutions for UPS and XPS spectra were 0.1 and 0.5 eV, respectively.

AFM, C-AFM and KPFM

AFM studies of thin films were performed with the Cypher S microscope (Asylum Research, Oxford Instruments) in tapping mode under ambient conditions using a silicon cantilever (AC240TS-R3) with a resonant frequency of around 70 kHz. C-AFM studies of thin films were performed with the Cypher ES microscope (Asylum Research, Oxford Instruments). Soft Pt/Cr-coated silicon probes were used for topography and current maps in contact mode. The current maps were obtained by constantly biasing the substrate while keeping the scanning AFM probe at the ground. KPFM measurement was performed in ambient conditions using Bruker FastScan AFM instrument in the PeakForce KPFM mode. The scanning rate for the KPFM measurements was maintained at 16 Hz.

Statistics

The data are normalized by dividing the maximum value. The data of electrical performance are presented by mean ± s.d. The data of electrical performance are tested for at least three samples and then statistically analysed to obtain mean values and s.d.

Data availability

All relevant data are contained in the article and its Supplementary Information or are available from the corresponding authors on request. Source data are provided with this paper.

41. Lu, Y. et al. Persistent conjugated backbone and disordered lamellar packing impart polymers with efficient n-doping and high conductivities. *Adv. Mater.* **33**, 2005946 (2021).
42. Shi, K. et al. Toward high performance n-type thermoelectric materials by rational modification of BDPPV backbones. *J. Am. Chem. Soc.* **137**, 6979–6982 (2015).
43. Yan, X. et al. Approaching disorder-tolerant semiconducting polymers. *Nat. Commun.* **12**, 5723 (2021).
44. Wang, X.-Y. et al. Density of states engineering of n-doped conjugated polymers for high charge transport performances. *Adv. Mater.* **35**, 2300634 (2023).
45. Li, F., Werner, A., Pfeiffer, M., Leo, K. & Liu, X. Leuco crystal violet as a dopant for n-doping of organic thin films of fullerene C₆₀. *J. Phys. Chem. B* **108**, 17076–17082 (2004).
46. Wei, P., Oh, J. H., Dong, G. & Bao, Z. Use of a 1H-benzimidazole derivative as an n-type dopant and to enable air-stable solution-processed n-channel organic thin-film transistors. *J. Am. Chem. Soc.* **132**, 8852–8853 (2010).
47. Shi, K. et al. A novel solution-processable n-dopant based on 1,4-dihydropyridine motif for high electrical conductivity of organic semiconductors. *Adv. Electron. Mater.* **3**, 1700164 (2017).
48. Sirringhaus, H. Device physics of solution-processed organic field-effect transistors. *Adv. Mater.* **17**, 2411–2425 (2005).
49. Paterson, A. F. et al. Impact of the gate dielectric on contact resistance in high-mobility organic transistors. *Adv. Electron. Mater.* **5**, 1800723 (2019).
50. Olthof, S. et al. Ultralow doping in organic semiconductors: evidence of trap filling. *Phys. Rev. Lett.* **109**, 176601 (2012).
51. Fratini, S., Nikolka, M., Salleo, A., Schweicher, G. & Sirringhaus, H. Charge transport in high-mobility conjugated polymers and molecular semiconductors. *Nat. Mater.* **19**, 491–502 (2020).
52. Günther, A. A., Sawatzki, M., Formánek, P., Kasemann, D. & Leo, K. Contact doping for vertical organic field-effect transistors. *Adv. Funct. Mater.* **26**, 768–775 (2016).
53. Xu, Y. et al. Planar-processed polymer transistors. *Adv. Mater.* **28**, 8531–8537 (2016).
54. Gu, G., Kane, M. G. & Mau, S. C. Reversible memory effects and acceptor states in pentacene-based organic thin-film transistors. *J. Appl. Phys.* **101**, 014504 (2007).

Acknowledgements We acknowledge the High-Performance Computing Platform of Peking University for supporting the computational work. We acknowledge Molecular Materials and Nanofabrication Laboratory (MMNL) at the College of Chemistry and Molecular Engineering and Electron Microscopy Laboratory of Peking University for the use of instruments. We thank beamline BL14B1 (Shanghai Synchrotron Radiation Facility) for providing beam time. We thank Y. Lu from the College of Chemistry and Molecular Engineering, Peking University, and C.-Y. Yang from the Department of Science and Technology, Linköping University, for constructive advice. We thank P. Li and W. Sun from the School of Materials Science and Engineering, Peking University, for device fabrication. We thank Y. Gao from the Institute of Modern Optics at the School of Physics, Peking University, for the C-AFM measurement. We thank Z. Wang from Max-Planck-Institut für Kohlenforschung for the photoexcitation calculation. We thank Z. Ji and C.-A. Di from Institute of Chemistry, Chinese Academy of Sciences, for the KPFM measurement. We thank Ningbo Boya Poly Advanced Materials Co. Ltd. for providing flexible polyimide substrates (CPI-TDS-C008). This work is supported by the National Natural Science Foundation of China (22020102001, 22335002 and 22071007), National Key R&D Program of China (2022YFB3602802) and Natural Science Foundation of Beijing Municipality (Z220025).

Author contributions J.P. designed the project and experiments and supervised the work. X.-Y.W. and Y.-F.D. synthesized iPADs. X.-Y.W., Y.-F.D., Y.-F.H., H.-T.W., C.-X.H. and M.X. characterized the light-triggered doping process of iPADs. C.-K.P., Y.-H.L. and N.-F.L. carried out the DFT calculation. X.-Y.W., Y.-F.D., Y.-Y.Z., X.-Y.Z., Y.-S.C., Z.-H.X., C.-K.P. and Y.-C.X. fabricated the light-triggered doping devices. Z.-D.Y. and Q.-Y.L. carried out XPS and UPS characterization. X.-Y.W. carried out the grazing incidence wide-angle X-ray scattering characterization and data analysis. Y.-Y.Z. carried out the C-AFM characterization. X.-Y.Z. carried out the KPFM characterization. X.-Y.Z. and L.D. fabricated the flexible devices. X.-Y.W., Z.-F.Y., Y.-Q.Z., J.-Y.W. and J.P. wrote the manuscript. All authors reviewed and commented on the manuscript.

Competing interests The authors declare no competing interests.

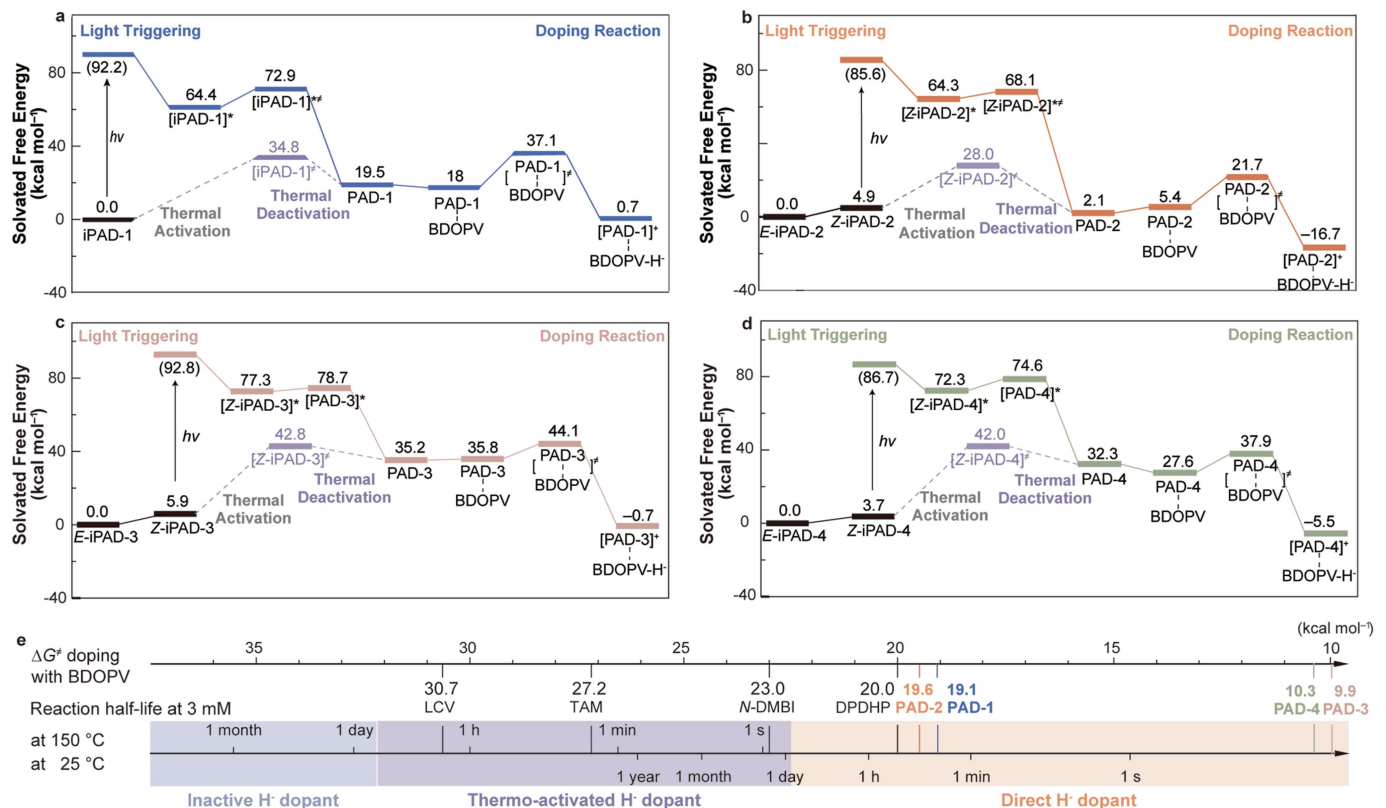
Additional information

Supplementary information The online version contains supplementary material available at <https://doi.org/10.1038/s41586-025-09075-y>.

Correspondence and requests for materials should be addressed to Jian Pei.

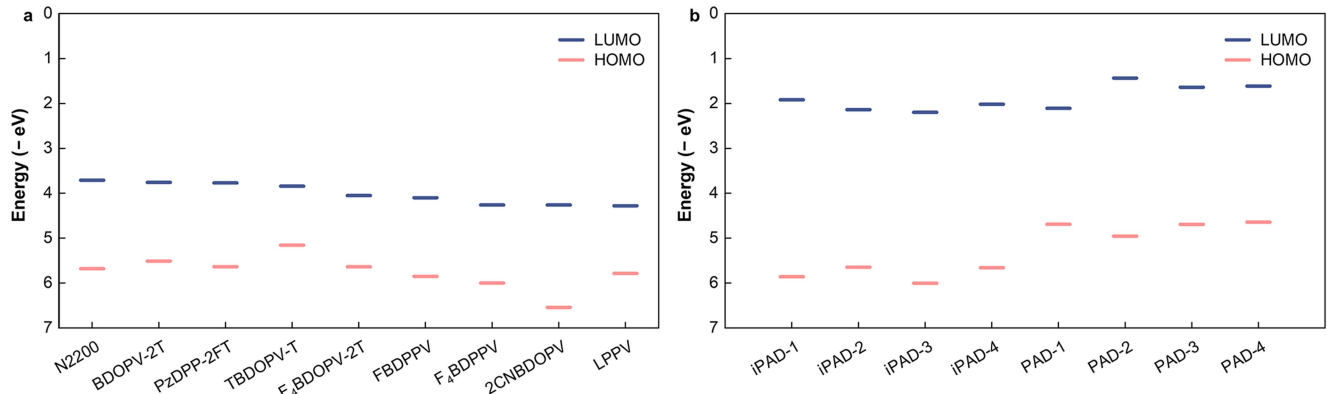
Peer review information *Nature* thanks Julianna Panidi, Shun Watanabe and the other, anonymous, reviewer(s) for their contribution to the peer review of this work.

Reprints and permissions information is available at <http://www.nature.com/reprints>.



Extended Data Fig. 1 | DFT calculation. **a–d**, Gibbs free energy profiles of the photoactivation, thermoactivation and doping processes of iPAD-1 (a), iPAD-2 (b), iPAD-3 (c) and iPAD-4 (d). **e**, The activation Gibbs free energy and half-life of doping reaction between model molecular benzodifurandione-based oligo(*p*-phenylene vinylene) (BDOPV) with iPAD-1, PAD-1, leuco crystal violet (LCV)⁴⁵, triaminomethane-based dopant (TAM)⁹, (4-(1,3-dimethyl-2,3-dihydro-1*H*-benzimidazol-2-yl)phenyl)dimethylamine (*N*-DMBI)⁴⁶ and 4-(4-methoxyphenyl)-1-methyl-2,6-di-phenyl-1,4-dihdropyridine (DPDHP)⁴⁷. The detailed energy profiles for hydride-transfer reactions and the molecule structures of BDOPV and dopants are presented in Supplementary Fig. 3. iPAD-1 is taken as an example to explain the light-triggered doping process. First, the inactive dopant iPAD-1 shows a low-lying highest occupied molecular orbital (HOMO) and high activation energy for hydride donation (Extended Data Fig. 2), suggesting that iPAD-1 could not dope polymers through electron transfer and hydride transfer. Second, the inactive dopant iPAD-1 could be

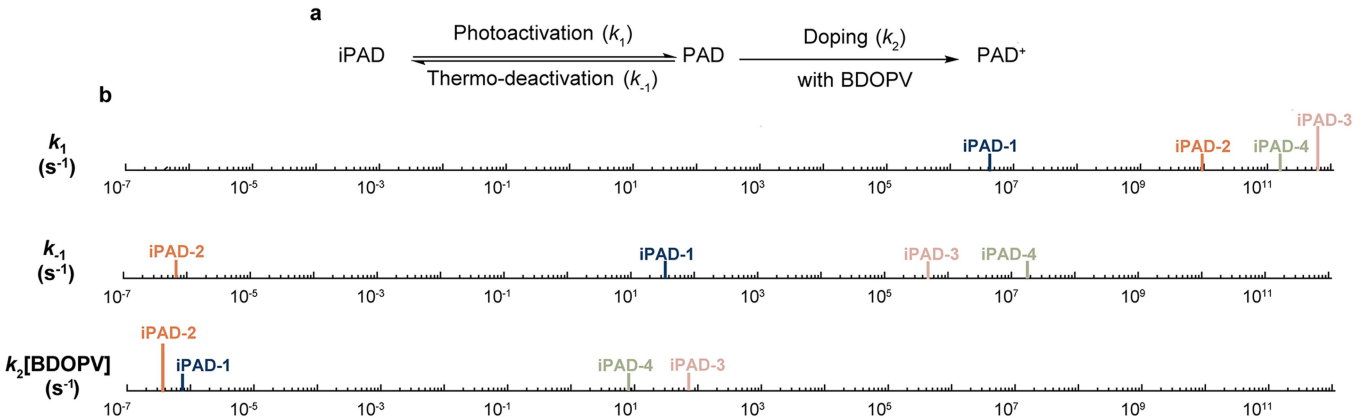
activated into PAD-1 through an excited state of 6π-electrocyclization after UV light exposure. Such transformation requires an activation energy of only 8.5 kcal mol⁻¹ (Extended Data Fig. 1a), which is almost instant at room temperature. However, the activation Gibbs free energy of thermocyclization of iPAD-1 is as high as 34.8 kcal mol⁻¹, indicating that thermal activation is infeasible. Third, the activated dopant PAD-1 could readily dope OSCs for transforming into a more stable aromatic structure, [PAD-1]⁺, through hydride transfer. The activation energy of doping BDOPV by PAD-1 is only 19.1 kcal mol⁻¹, allowing the reaction to occur at room temperature at a reasonable rate even at a low concentration (3 mM). Finally, the reverse reaction, hydride transfer from doped BDOPV back to PAD-1, has a high energy barrier of 36.4 kcal mol⁻¹, making the doping process irreversible, which is also supported by the UV-vis spectra in Supplementary Fig. 5. The UV-vis spectra of iPAD-1-doped 2CNBDOPV remain unchanged after being stored for 2 days. These results indicate that iPAD can serve as photoactivable dopants for phototriggered doping of OSCs.



Extended Data Fig. 2 | HOMO and LUMO levels. **a,b,** HOMO and LUMO levels of OSCs, iPADs and PADs. Inactive dopant (iPAD-1) shows a low-lying HOMO orbital at ~ -5.86 eV, much lower than LUMO levels of typical OSCs (in the range of -4.3 to -3.7 eV), suggesting that iPAD-1 cannot dope polymers through electron transfer. With an extremely weak hydride-donating ability, iPAD-1 cannot dope OSCs through hydride transfer. The spectra of FBDPPV/iPAD-1 blend solution remain unchanged even at high annealing temperatures of

120 °C, suggesting that the iPAD-1 cannot dope OSCs by thermoactivation (Fig. 2b). After light triggering, iPAD-1 can be transformed into the activated dopant (PAD-1). The LUMO levels of OSCs are still higher than the HOMO levels of PAD-1, which means that electron transfer cannot spontaneously occur. However, PAD with a dihydropyridine motif can readily aromatize to PAD⁺ through hydride transfer. This hydride-transfer process has been proved by UV-vis-NIR spectra in Supplementary Figs. 1, 5 and 6.

Article

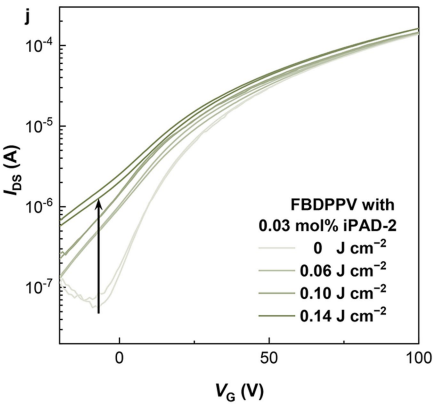
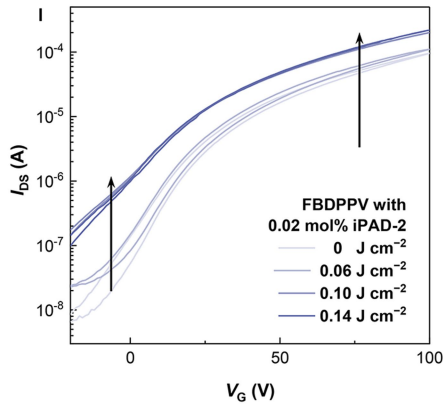
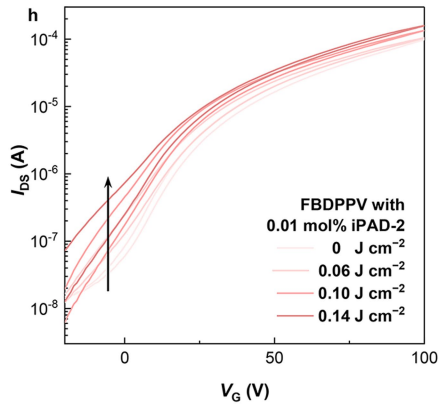
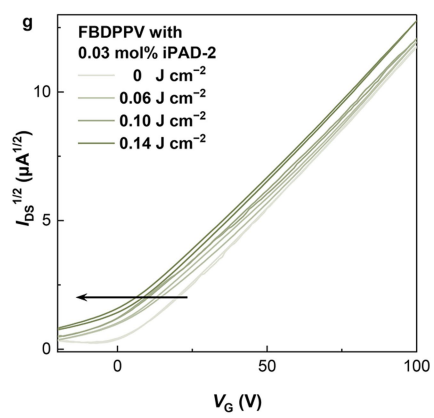
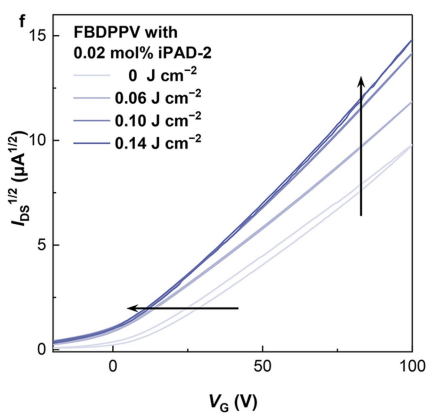
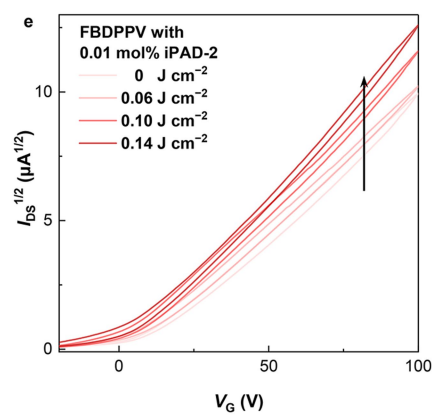
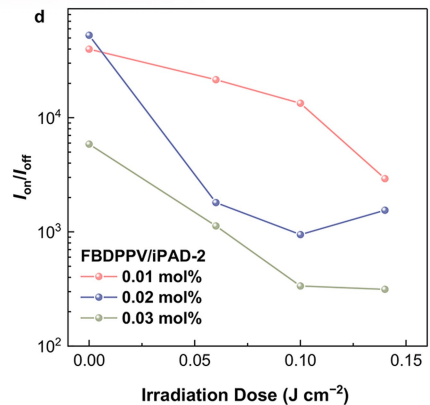
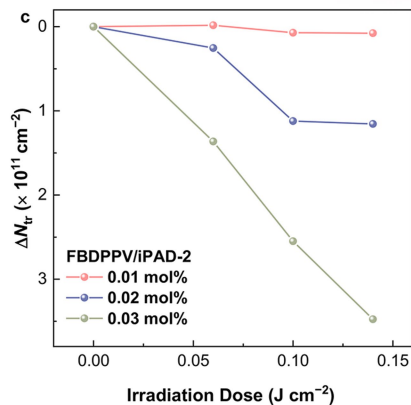
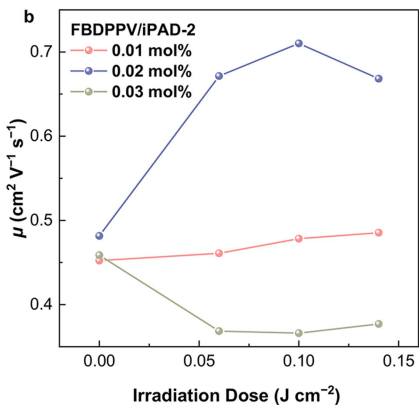
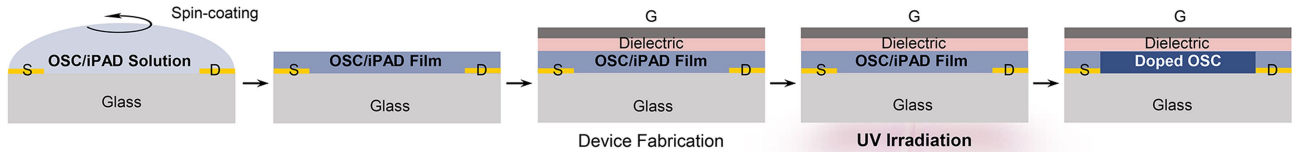


Extended Data Fig. 3 | Examination of iPADs for n-doping of OSCs.

a, Light-triggered doping process. **b**, Rate constant of the photoactivation (k_1), thermodeactivation (k_{-1}) and doping with BDOPV (k_2). k_1 , k_{-1} and $k_2[\text{BDOPV}]$ are calculated from the activation Gibbs free energy by Eyring equation (Supplementary Table 3). The concentration of BDOPV is $10^{-5} \text{ mol l}^{-1}$. On the basis of our DFT calculation and experiment, the possible doping process is a two-step mechanism with a reversible PAD formation and an irreversible hydride-transfer process. The rate constants of the photoactivation processes of four iPADs are higher than 10^6 s^{-1} , indicating the instant transformation from iPADs to PADs after UV irradiation. For iPADs, the rate constant of thermodeactivation follows $k_{-(\text{PAD-2})} < k_{-(\text{PAD-1})} \ll k_{-(\text{PAD-3})}$ and $k_{-(\text{PAD-4})}$, indicating that the concentrations of PAD-3 and PAD-4 are extremely low after UV irradiation. The low concentration of PADs results in low collision probability with BDOPV, impeding the

doping reaction. Therefore, the light-triggered doping rates follow the tendency iPAD-2 > iPAD-1 > iPAD-3 and iPAD-4, which has been proved by UV-vis-NIR spectra. The rate of hydride-transfer reactions between representative electrophile tritylium cation ($(\text{MeO})_3\text{Tr}^+$ and iPAD-3 or iPAD-4 is slower than iPAD-1 and iPAD-2 (Supplementary Fig. 14). The same conclusion has also been proved by the absorption spectra of FBDPPV/iPAD blend solutions (Fig. 3a,b and Supplementary Fig. 15). These results demonstrate that thermodeactivation substantially impedes the photoactivated doping reaction between iPADs and OSCs. For PAD-1 and PAD-2, the smaller interplanar angles and weaker antiaromaticity can stabilize PADs, which decreases the rate of thermodeactivation and further enhances the doping reaction (Supplementary Figs. 17 and 18).

a Channel doping FET process

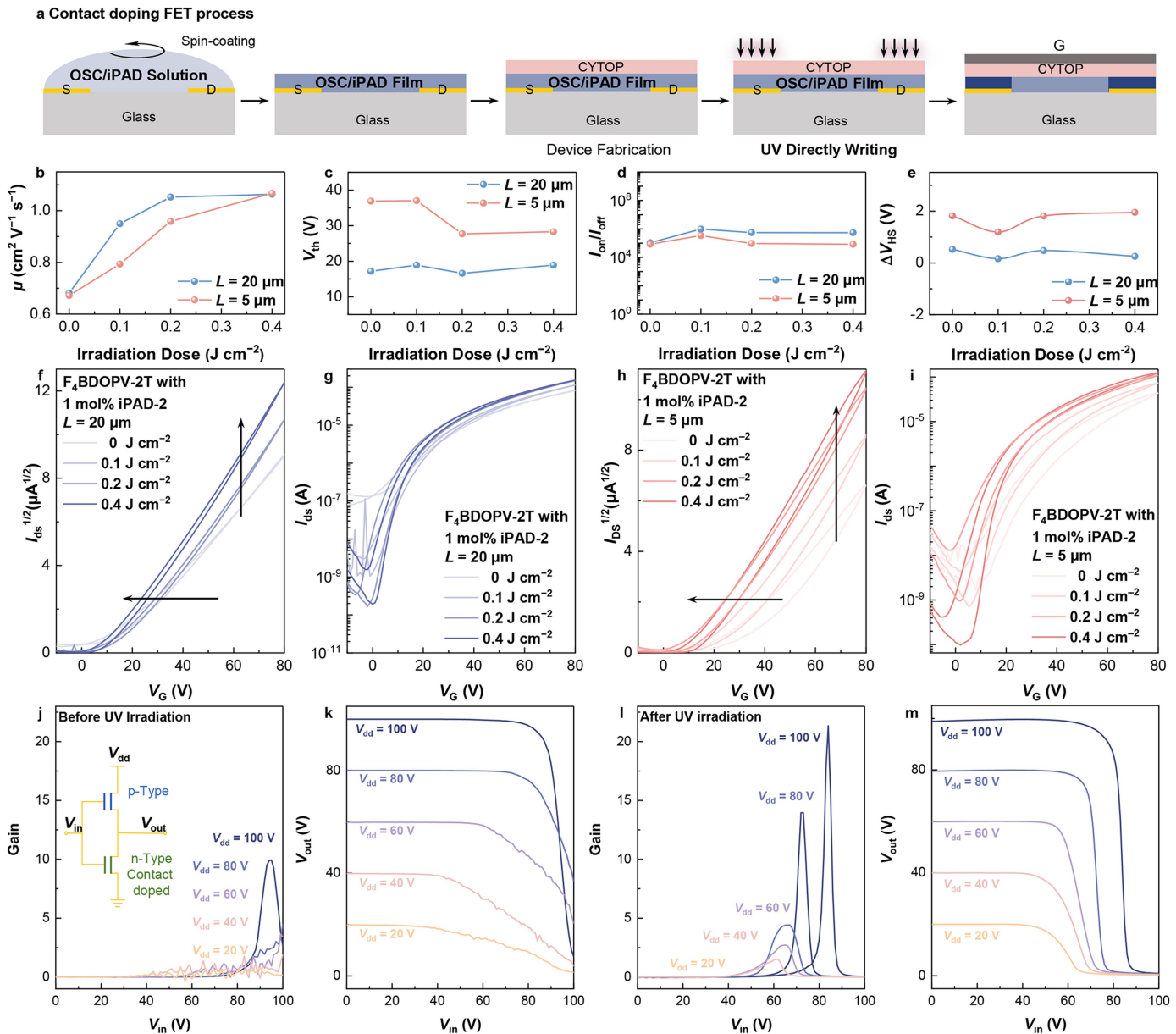


Extended Data Fig. 4 | See next page for caption.

Article

Extended Data Fig. 4 | Channel-doped FETs. For most OSCs, the carrier transport in FETs is a hopping process owing to weak van der Waals interaction among molecules, as well as structural and energetic disorders⁴⁸. Furthermore, the charge trapping at the OSC–dielectric interface could hinder charge transport, decreasing carrier mobility notably⁴⁹. Selectively doping the channels of FETs has been reported to effectively fill the carrier traps and lower the energy barrier of carrier transport, further decreasing the threshold voltages and improving the mobilities of FET devices⁴⁰. Channel-doping of FET devices can be realized by selectively light triggering our dopants. At low dopant concentrations, the mobilities of FETs increase with doping ratio owing to the fill of carrier traps⁵⁰, with the increase of on-state current and decrease of V_{th} . At high dopant concentrations, the carriers are accumulated in channel, whereas at large negative voltages, the doped channel is increasingly depleted⁵. This unwanted carrier accumulation increases the off-current and decreases the on–off ratio. Furthermore, at high dopant concentrations, Coulomb interaction between carriers and dopant counterions brings about more energetic disorders, further decreasing the mobilities of FETs⁵¹. **a**, Fabrication process of light-triggered doping FETs at channels. OSC/iPAD blend solution is spin-coated on the substrate with patterned source and drain electrodes.

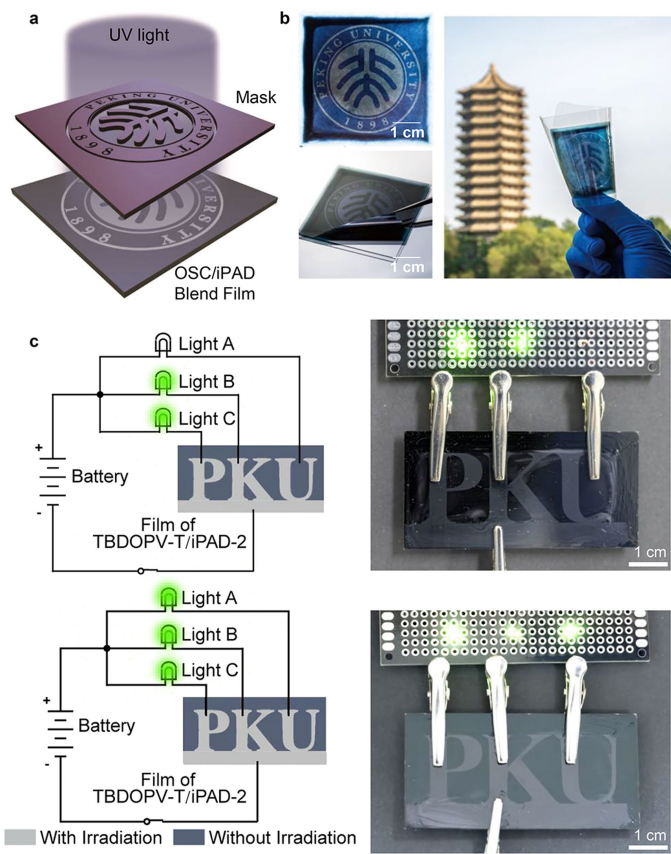
The dielectric layer and gate electrode are sequentially deposited on OSC/iPAD blend films. FETs are exposed to UV irradiation from the backside, leading to selective doping OSCs at channels. Channel-doped FETs are fabricated using FBDPPV mixed with different molar ratios of iPAD-2 as the active layer. A low doping molar ratio (0.01–0.03 mol%) of iPAD-2 and low irradiation dose (<0.15 J cm⁻²) are selected to optimize the performance of FET devices to achieve the off-state of devices after doping. $W/L = 20$. **b–d**, Mobilities (**b**), relative surface trap densities (**c**) and on–off ratios as a function of UV exposure doses (**d**). Points, mean; $n = 5$ independent samples. **e,h**, $I_{DS}^{1/2}$ as a function of V_G (**e**) and I_{DS} as a function of V_G (**h**) for FETs using FBDPPV/0.01 mol% iPAD-2 blend films as the active layer. **f,i**, $I_{DS}^{1/2}$ as a function of V_G (**f**) and I_{DS} as a function of V_G (**i**) for FETs using FBDPPV/0.02 mol% iPAD-2 blend films as the active layer. **g,j**, $I_{DS}^{1/2}$ as a function of V_G (**g**) and I_{DS} as a function of V_G (**j**) for FETs using FBDPPV/0.03 mol% iPAD-2 blend films as the active layer. The drain voltage is 100 V in the saturated regime. Output curves, gate voltage dependence mobilities, V_{DS} dependence transfer curves, threshold voltages and transconductances of channel-doped devices are shown in Supplementary Figs. 30–37. All polymer transistors exhibit reliable n-type carrier transport.



Extended Data Fig. 5 | Contact-doped FETs. High contact resistance at the metal and OSC interface prevents efficient charge injection and extraction, fundamentally limiting the device performance⁴⁰. Doping at contact can turn the Schottky barrier into a tunnelling barrier and passivate high-density traps at contacts, further improving charge injection at the metal–semiconductor interface. Therefore, contact doping of FET devices can reduce contact resistance and decrease the energy barrier for carrier injection and extraction, further increasing carrier mobility and decreasing V_{th} . In our contact-doped FETs, the doping reaction is confined into contacts and does not substantially increase the carrier concentration in the OSC channel. As a result, contact doping has minimal impact on the on–off ratio of devices. Furthermore, n-type contact doping promotes hole injection barrier and reduces leakage current, thereby reducing the off-state current of devices^{52,53}. **a**, Fabrication process of light-triggered doping FET at contacts. OSC/iPAD solution is spin-coated on the substrate with patterned source and drain electrodes. A UV transparent polymer CYTOP is spin-coated on OSC/iPAD blend films as the dielectric layer. FETs are selectively exposed to UV light at contacts using laser direct writing and then the gate electrode is deposited on CYTOP. FETs are fabricated using $F_4\text{BDOPV-2T}$ mixed with 1 mol% iPAD-2 as the active layer. **b–e**, Mobilities (**b**), threshold voltages (**c**), on–off ratios (**d**) and hysteresis windows as a function of

UV exposure doses (**e**). Points, mean; $n = 5$ independent samples. **f,g**, $I_{ds}^{1/2}$ as a function of V_G (**f**) and I_{ds} as a function of V_G (**g**) for FETs with channel length $L = 20\text{ }\mu\text{m}$ and channel width $W = 400\text{ }\mu\text{m}$. **h,i**, $I_{ds}^{1/2}$ as a function of V_G (**h**) and I_{ds} as a function of V_G (**i**) for FETs with $L = 5\text{ }\mu\text{m}$ and channel width $W = 100\text{ }\mu\text{m}$. The drain voltage is 80 V in the saturated regime. Output curves, gate voltage dependence mobilities and transconductances of channel-doped devices are shown in Supplementary Figs. 38–40. All polymer transistors exhibit reliable n-type carrier transport. Contact doping can effectively eliminate nonideal behaviours and increase the mobility of devices. FETs with shorter channel lengths exhibit more pronounced hysteresis than those with longer channels, which we attribute to the increased carrier trapping within channel⁵⁴ (Supplementary Fig. 41). Although contact doping reduces contact resistance and lowers the energy barriers for carrier injection and extraction, it does not mitigate carrier trapping within channel. Consequently, the hysteresis persists despite contact doping (Supplementary Fig. 42). **j,k**, Gain values of an inverter at different voltages before UV irradiation (**j**) and after 0.4 J cm^{-2} UV irradiation (**k**) on contacts. **l,m**, Static switching characteristics of an inverter before UV irradiation (**l**) and after 0.4 J cm^{-2} UV irradiation (**m**) on contacts. $F_4\text{BDOPV-2T}/1\text{ mol\% iPAD-2}$ blends are used as the n-channel materials. DPP-TVT is used as the p-channel material.

Article



Extended Data Fig. 6 | Application of light-triggered doping processes.

a, Schematic of regionally controlled doping of OSCs as conducting regions through a photomask. OSC/iPAD blend film is fabricated by drop-casting on the substrate and is then selectively light triggered through a photomask.

b, Photographs of the region-controlled doped OSC film on a flexible polyimide substrate. The grey area is the conductive region and the dark-blue area is the non-conductive region. **c**, Schematics of the region-controlled doping OSCs to construct simple circuits by UV exposure through a photomask. The film is fabricated by drop-coating TBDOPV-T/iPAD-2 blend solution on the substrate. The grey area is the conductive region and the dark area is the non-conductive region. When the patterned P and K letters (exposed area) are connected to the circuit, lights B and C are turned on, whereas light A remains off. Connecting the patterned P, K and U letters results in a conductive pathway and further turns on all three lights (Supplementary Video 1).